

PCCP

Accepted Manuscript



This is an *Accepted Manuscript*, which has been through the Royal Society of Chemistry peer review process and has been accepted for publication.

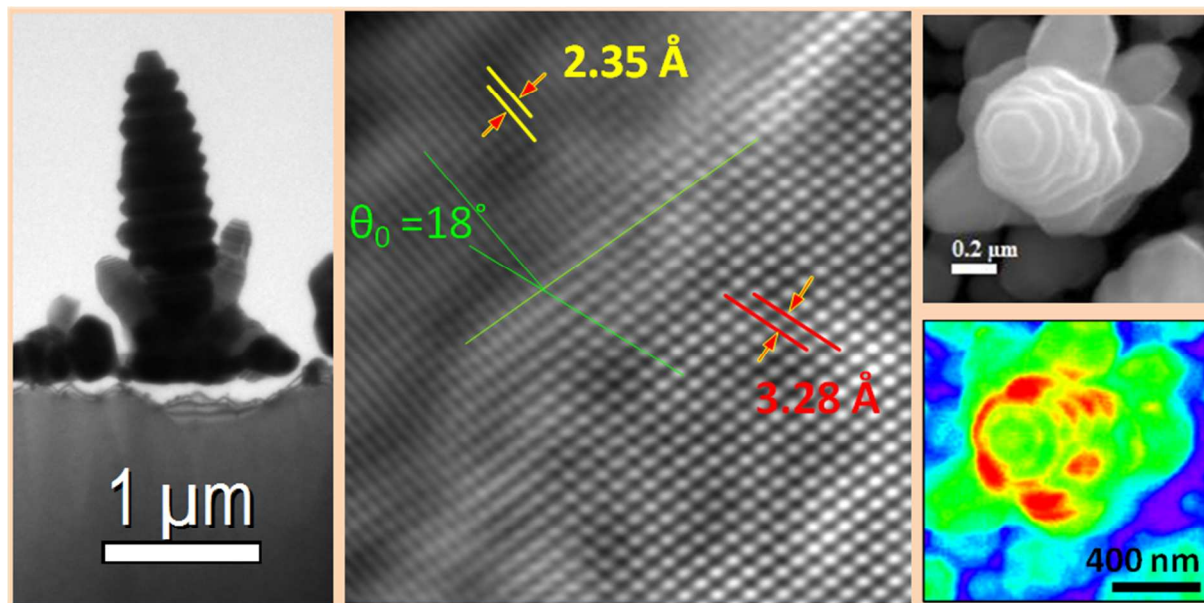
Accepted Manuscripts are published online shortly after acceptance, before technical editing, formatting and proof reading. Using this free service, authors can make their results available to the community, in citable form, before we publish the edited article. We will replace this *Accepted Manuscript* with the edited and formatted *Advance Article* as soon as it is available.

You can find more information about *Accepted Manuscripts* in the [Information for Authors](#).

Please note that technical editing may introduce minor changes to the text and/or graphics, which may alter content. The journal's standard [Terms & Conditions](#) and the [Ethical guidelines](#) still apply. In no event shall the Royal Society of Chemistry be held responsible for any errors or omissions in this *Accepted Manuscript* or any consequences arising from the use of any information it contains.

Table of Contents

Dendritic silver nanostructures prepared by Galvanic displacement reaction on large-lattice-mismatched germanium substrate shows a new type of heteroepitaxial growth where significantly large lattice mismatch is accommodated by formation of low-energy asymmetric tilt boundaries.



Cite this: DOI: 10.1039/c0xx00000x

www.rsc.org/xxxxxx

ARTICLE TYPE

Tilt Boundaries Induced Heteroepitaxy for Chemically Grown Dendritic Silver Nanostructures on Germanium and Their Optical Properties

Tanmay Ghosh, Pabitra Das, Tapas Kumar Chini, Tapas Ghosh and Biswarup Satpati*

Received (in XXX, XXX) Xth XXXXXXXXXX 20XX, Accepted Xth XXXXXXXXXX 20XX

DOI: 10.1039/b000000x

Dendritic silver nanostructures were prepared by a simple dip-and-rinse galvanic displacement reaction directly on germanium surfaces. The formation and evolution of these dendrites were investigated using scanning electron microscopy (SEM), high-resolution transmission electron microscopy (HRTEM) and energy-dispersive X-ray spectroscopy (EDX). The present results clearly show a new kind of heteroepitaxy, where large lattice mismatch between silver and germanium is accommodated at the interface by the formation of low-energy asymmetric tilt boundaries. Over grown sample relax strain by introducing crystal defects. Additionally, employing cathodoluminescence (CL) spectroscopy and imaging in a field emission gun scanning electron microscope (FEG-SEM), we provide information of surface plasmon assisted photon emission from a stack of Ag hexagon nanostructure. Surface enhanced Raman scattering (SERS) study shows the suitability of such Ag nanodendrite structures to be used as SERS active substrate.

Introduction

In recent years, there is a tremendous progress in the design and fabrication of metallic nanostructures of complex geometry emphasizing the fine control of their morphological characteristics towards functional applications in optical, optoelectronics and magnetic devices.¹ For example, complexity of metallic nanostructures is suitable for their use as surface enhanced Raman scattering (SERS)-active substrates.²⁻⁵ The optical response of noble metal nanoparticles (NMNPs) is governed mainly by the collective oscillation of conduction electrons in NMNP, known as localized surface plasmon (LSP). LSP when excited resonantly with a particular wavelength of the exciting radiation can lead to considerable localized enhancement of the near-field amplitude at the nanostructured metal surface, especially at the regions of sharp edges, corners, tips and or apexes allowing electromagnetic (EM) energy to be confined at the subwavelength length scale. Regions of strongest enhancement due to this 'electromagnetic effect', known as 'hot spots', are responsible for large enhancement in SERS signal and have several interesting effects, such as enhanced fluorescence,⁶ enhanced photocarrier generation,⁷ that can have potential applications in biosensing, photovoltaics, and single molecule detection. In this context, metal dendritic nanostructures are of one type of attractive complex structures where apexes of dendritic aggregates are expected to provide more favourable centres of hot spots⁸ than the nanosphere or nanowire morphology of the same metals. Consequently, a good understanding of the process and parameters controlling the dendrite formation is crucial for achieving the design of novel dendritic nanostructures with desired properties. Among various

inorganic metals, the preparation of Ag dendrite has been widely investigated. Till date, quite a few methods are employed to fabricate dendritic Ag structures. Electrochemical deposition,⁹⁻¹² galvanic replacement reaction,^{9,13-17} solvothermal or hydrothermal reaction,¹⁸⁻²⁰ organic reagent reduction using surfactant,²¹⁻²³ ultrasonic-assisted reduction,²⁴ ultraviolet irradiation reduction,²⁵ and template method²⁶ to name a few. Among these methods, galvanic replacement reaction has attracted great interest due to its simplicity of operation, cost effectiveness and high throughput. The electrical potential difference between two metals is the driving force for the galvanic replacement reaction. Yu and co-workers have reported the growth of heterogeneous Ag-Cu dendrites on a Cu foam substrate.²⁷ Despite a large number of reports on the preparation and theoretical studies of the dendritic nanostructures, it has still been a significant challenge to discover common mechanisms underlying their formation such as nucleation and growth.

The growth of Ag on Ge (100) is of particular interest which includes at least eight different phases, some of which have novel, non equilibrium coexistence regions in the phase diagram.²⁸ In this work, we demonstrate the formation of Ag nanodendrite structure depending on the duration of contact of AgNO₃ solution on a native oxide covered Ge (100) surface. Our detail cross-sectional HRTEM based analysis for the Ag-Ge interface shows that nucleation of Ag nanocrystallites gives rise to a tilted heteroepitaxy that promotes the growth of lattice-mismatched structures without introducing misfit dislocations at the interface which propagate to the upper layer. The novelty of this simple growth process results in a new kind of heteroepitaxy where large lattice mismatch (about 27.7 % for the present case

of Ag/Ge interface) can be accommodated by the formation of low-energy asymmetric tilt boundaries. Overgrown sample relaxes strain by introducing several crystal defects. Employing cathodoluminescence (CL) spectroscopy and imaging in a field emission gun scanning electron microscope (FEG-SEM), we provide information of surface plasmon assisted photon emission both in spectral and spatial domain under local excitation from a stack of Ag hexagon nanostructure. Additionally, through surface enhanced Raman scattering (SERS) study we show the suitability of such Ag nanodendrite structures to be used as SERS active substrate.

EXPERIMENTAL SECTION

Growth and Specimen Preparation for TEM

Silver nanostructures were grown at concentrations around 1 mM of AgNO₃ (aq) at room temperature on flat native oxide-coated germanium surfaces by Galvanic displacement reactions. Germanium-germanium bonds in the crystal lattice acting as the reducing agent for the Ag⁺ ions in the solution leads to Ag and simultaneous oxidation of Ge to Ge⁴⁺ by spontaneous redox reaction. The resulting Ge⁴⁺ product, germanium oxide, is water soluble and remains in the solution.²⁸ After a desired time of reaction, Ge substrate with grown Ag nanostructures was taken out from the solution. Sample for transmission electron microscopy (TEM) in plan-view and cross-sectional mode were prepared with special care. It was known that these nanostructures can be easily isolated by sonication of a sample in methanol.²⁹ For plan-view TEM a few discs of 3 mm in diameters were cut from a one side mirror polished Ge wafer. They were further thinned by polishing back side (unpolished side) using silicon carbide papers and emery papers, up to the thickness of about 80 μm. The thickness of the discs were further reduced at the central portion, using a dimple grinder (M/s Gatan make), to a thickness of about 20 μm. Dimpled discs were then subject to ion milling using Ar ions in a precision-ion-polishing system (PIPS, Gatan, Pleasanton, CA) till a fine perforated hole was made at the centre of the disc, enabling the adjacent area of the hole to be electron transparent. Silver nanostructures were then grown on one side (mirror polished side) by floating the electron transparent discs on AgNO₃ solution. In this way we avoid any changes in topography in the process of TEM sample preparation of these metal nanoparticles as they are very weakly bound to the Ge substrates. For cross-sectional TEM (XTEM) measurements metal nanoparticles were grown on two similar 2mm × 4mm pieces and then bonded face to face. Specimens were then prepared using the standard method of mechanical thinning and double dimpling with final thinning using a PIPS. The ion polishing was carried out at 3.0 keV energy without liquid nitrogen cooling followed by a 1.2 keV cleaning process. For TEM observation, specimens were aligned on [110] zone axes.

TEM Characterization

The Transmission electron microscopy (TEM) analysis was carried out using FEI, Tecnai G² F30, S-Twin microscope operating at 300 kV equipped with a Gatan Orius CCD camera.

The TEM is also equipped with high-angle annular dark field scanning transmission electron microscopy (STEM-HAADF) mode with a HAADF detector from Fischione (Model 3000). The compositional analysis was performed by energy dispersive X-ray spectroscopy (EDS, EDAX Inc.) attachment on the Tecnai G² F30.

CL Measurements

CL spectroscopy and imaging was performed on isolated faceted structure in a ZEISS SUPRA40 SEM equipped with the Gatan MonoCL3³⁰ cathodoluminescence system. All the CL data presented in this paper were recorded with an electron acceleration voltage of 30 kV and beam current of about 15 nA with a beam diameter of ~5 nm. The CL system in conjunction with the SEM can be operated in two modes, namely, monochromatic (mono) and panchromatic (pan). In the monochromatic mode, the focused e-beam is either scanned over the sample or positioned on a desired spot while the emitted light from the sample passing through the monochromator allows the emission spectra to be recorded serially in the range 300–600 nm for the high sensitivity photomultiplier tube detector (HSPMT) used in the present case. The spectral step of 4 nm and a dwell time of 0.25s for a band-pass of ~11 nm were maintained while collecting the CL spectra in the present experiment. The monochromatic photon map is then built up at a selected peak wavelength of the CL spectrum by scanning the e-beam over the sample. For each e-beam position, the luminescence is collected over the entire sample. The bright pixels correspond to the areas where the strongly excited plasmon mode emits the photons. When adding all the position dependent partial maps, obtained for each e-beam position, we obtain a full CL map of the plasmon mode associated with a particular wavelength. In the panchromatic mode of CL operation, the monochromator is bypassed and all the emitted wavelengths are collected. The contrast of the pan-CL image is determined by the variation of the integrated photon counts at each pixel in the sensitivity range of the HSPMT detector. CL image is proportional to the radiative local density of optical states (LDOS) of the plasmonic structure.^{31,32} All the experimentally acquired images (both monochromatic and panchromatic) are of (160 × 160) pixels and each pixel corresponds to a length of 8 nm.

RESULTS AND DISCUSSION

Silver nano-inukshuk were grown at 1mM concentrations of AgNO₃ (aq) at room temperature on flat and native oxide-coated germanium surfaces for 4h as shown in the low magnification SEM image of Figure 1a. Figures 1b-c are high magnification SEM images of different structures evolved after completion of growth for 4h. The nano-inukshuks appear as ~ 650 nm diameter stacked hexagons with facets (Figure 1c), and can grow up to 3 or more microns in length and the hexagonal plates themselves are 120-150 nm thick (see Figure 2a). Growth of nano-inukshuks sprouting from the Ge surface is best understood from cross-sectional TEM image in Figure 2a and STEM-HAADF image in Figure 2b.

Cite this: DOI: 10.1039/c0xx00000x

www.rsc.org/xxxxxx

ARTICLE TYPE

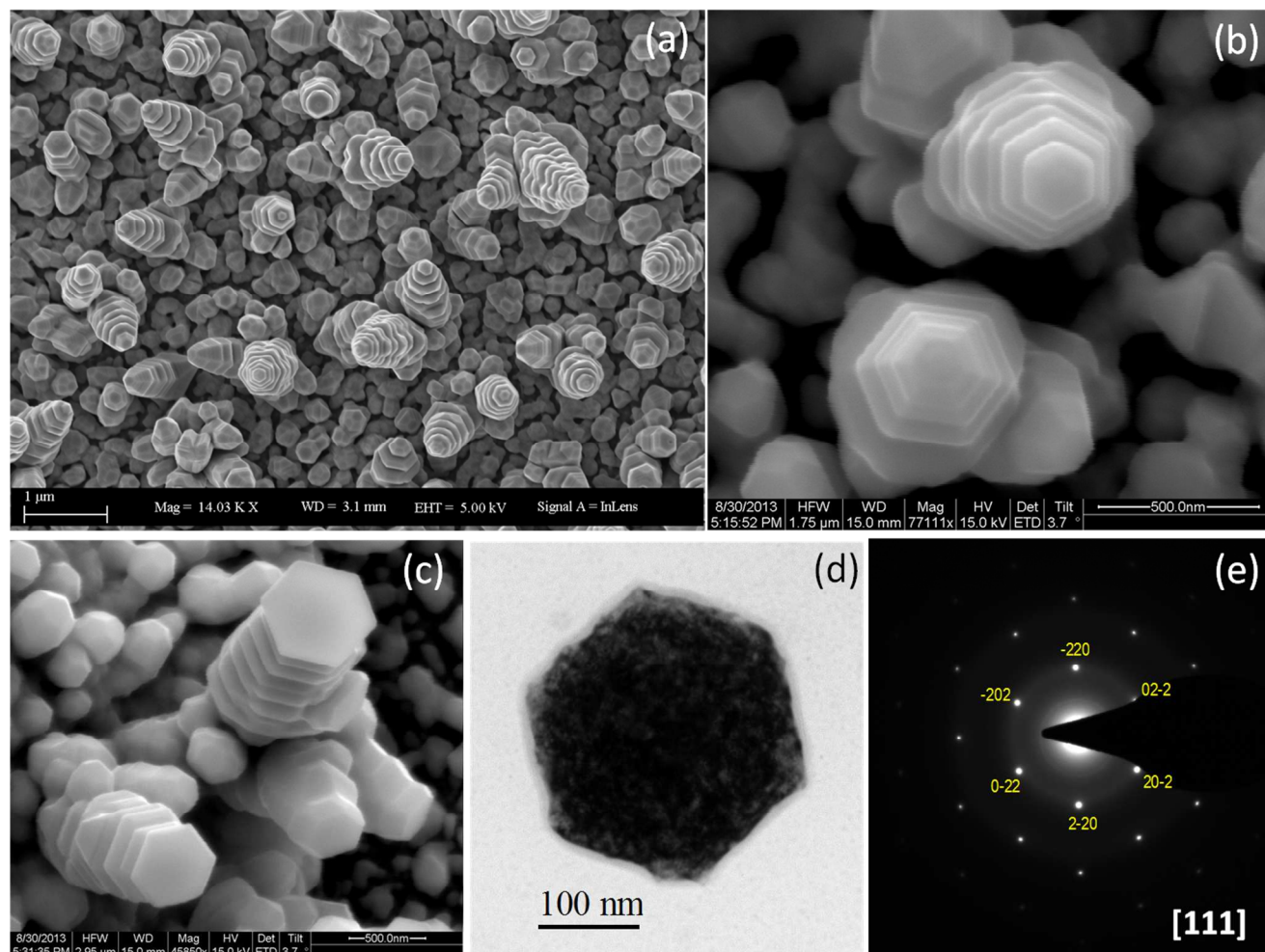


Fig. 1 (a) Low magnification SEM image showing overall morphology after silver deposition on Ge (100) n-type wafer for 4h, with 1 mM AgNO_3 . (b-c) Close-up of facets on the tips of silver metallic nano-inukshuks. (d) TEM of a silver hexagon isolated by sonication of silver nano-inukshuks in methanol. (e) [111] Zone-axis indexed selected area diffraction (SAED) pattern from hexagon isolated particle shown in (d).

5 In order to characterize the interface between Ag and Ge, XTEM
measurements were carried out. The XTEM image of a typical
dendrite nanostructure for 4h growth is shown in Figure 2a at low
magnification. The STEM-HAADF image of the same structure
is shown in Figure 2b. The XTEM sample was prepared by taking
10 two pieces one from as-grown nanostructures on Ge substrate
(lower part of image 2b) and other is the substrate where the
grown nanoparticles were removed from the substrate using
ultrasonic bath (upper part of image 2b). Interestingly nice nano-
patterned Ge substrate is produced in this way. EDX spectra

15 collected from area 1 and 2 as shown in Figure 2b is plotted in
Figure 2c. A small amount of Ge (~3 wt%) is observed from area
1 which may be due to water soluble germanium oxide formed in
this reaction and attached to Ag nanostructures. For
compositional analysis elemental mapping (Figure 2d) of the
20 structure using the STEM-HAADF-EDX technique was
performed using Ge-K and Ag-L energies which reveal that the
dendrite structures are made of Ag (magenta) and the substrate is
made of Ge (green).

Cite this: DOI: 10.1039/c0xx00000x

www.rsc.org/xxxxxx

ARTICLE TYPE

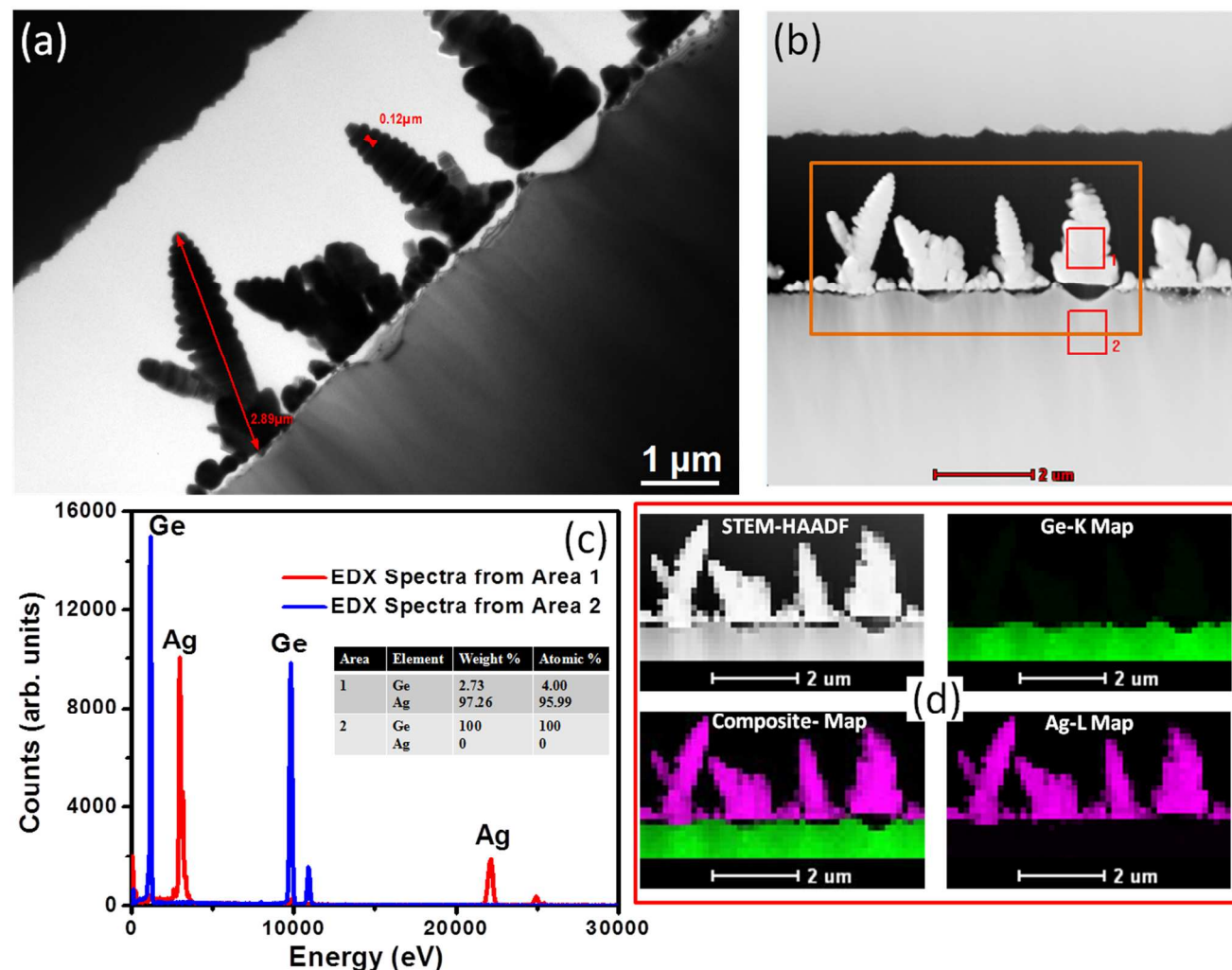


Fig. 2 (a) Typical low magnification XTEM image showing overall morphology after silver deposition on Ge (100) n-type wafer for 4h, with 1 mM AgNO₃. (b) STEM-HAADF image. (c) EDX spectra from region marked by area 1 and 2 in (b). (d) STEM-HAADF image from area marked by rectangle in (b) and corresponding EDX maps (Ge-K map, Ag-L map, and Ge-K and Ag-L combined map).

To carry out HRTEM measurements we have chosen the thinnest part of the cross-sectional TEM sample as shown in Figure 3. Selected area electron diffraction (SAED) pattern (see Figure 3a) from yellow dotted circles displays single crystal diffraction pattern from Ge substrate and from red dotted circle displays again single crystal diffraction pattern characteristic of the cubic Ag in addition with peaks due to stacking faults running parallel to each other. These stacking faults are evident from the HRTEM image and corresponding fast Fourier transform (FFT) pattern shown in inset of Figure 3c from an area few micron away from the interface (area 2 in Figure 3a marked by blue dotted box). We should mention here that there is an image rotation between two images (Figure 3a and 3c) in the microscope. Figure 3b is a HR-XTEM image from the interface between Ag nanodendrite and

Ge substrate (area 1 in Figure 3a marked by blue dotted box) which shows a connection between the dendrite and the substrate. Ag and Ge have 27.7% lattice mismatch but structurally similar (face centered cubic) materials. In inset of Figure 3b inverse FFT image of the coherent Ag(111)/Ge(111) interface shows that the Ag (111) planes are tilted by 312 mrad (~18°) relative to the (111) planes of the Ge matrix. In the FFT pattern of Figure 3d, the spots corresponding to Ge lattice spacing are marked by red circle and that corresponding to Ag lattice spacing are marked by yellow circle. It can be seen from the FFT pattern (Figure 3d) taken from the interface (as shown by yellow dotted square in 3b) that it is not simply a physical contact but rather like an epitaxial growth; both belong to the same crystal system (fcc). Fourier filtered image (inset of Figure 3b) shows fringe spacing of Ge as

0.328 nm, which is very close to the interplanar spacing of Ge (111). Another set of fringes nearly perpendicular to the Ge displays a fringe spacing of 0.235 nm, which matches well with the interplanar spacing of Ag (111).

In conventional hetero-epitaxial growth, lattice mismatch is accommodated through biaxial strain and interfacial misfit dislocations. However, Dodson et al³³ have shown that large lattice mismatch can be accommodated by formation of low-energy asymmetric tilt boundaries without producing a long-range stress field establishing the fact that asymmetric tilt boundaries present another possible source of low energy route toward accommodation of lattice mismatch in heteroepitaxial growth process. According to their model of accommodation of lattice mismatch, for an asymmetric tilt boundary, the effective mismatch goes to zero at an accommodation angle θ_0 defined by $a_0\varepsilon_0/a_1 = 1 - \cos\theta_0$, where ε_0 is the lattice mismatch and a_0 and a_1 are the unstrained lattice parameters of the two crystals. Applying such model, Dodson et al could explain the formation of

heterophase boundaries appearing in semicoherent α - Si_3N_4 precipitates grown *in situ* in a silicon matrix, where the $\text{Si}_3\text{N}_4(0001)$ planes are tilted by an angle of 5-10 mrad relative to the (111) planes of the Si matrix for a small lattice mismatch of 0.6% although this tilt angle was a small fraction of the accommodation angle ($\theta_0 \approx 110$ mrad) for the mismatch presented at $\text{Si}_3\text{N}_4(0001)/\text{Si}(111)$ interfaces. Interestingly, for the 4 hour grown Ag/Ge system of the present case, where the lattice mismatch (27.7%) is about an order of magnitude higher than the $\text{Si}_3\text{N}_4/\text{Si}$ system of Dodson et al, the asymmetric interfaces with a tilt of 18° (the tilt of Ag(111) planes relative to the (111) planes of the Ge matrix) are almost 50% of the calculated accommodation angle (36.86° for Ag/Ge system) showing much better agreement with the model than that observed in $\text{Si}_3\text{N}_4(0001)/\text{Si}(111)$ interfaces. Remaining strain is relaxed partially by introducing few misfit dislocation at the interface. However, overgrown sample introduce several defects (twining, stacking faults etc.) to relax the strain.

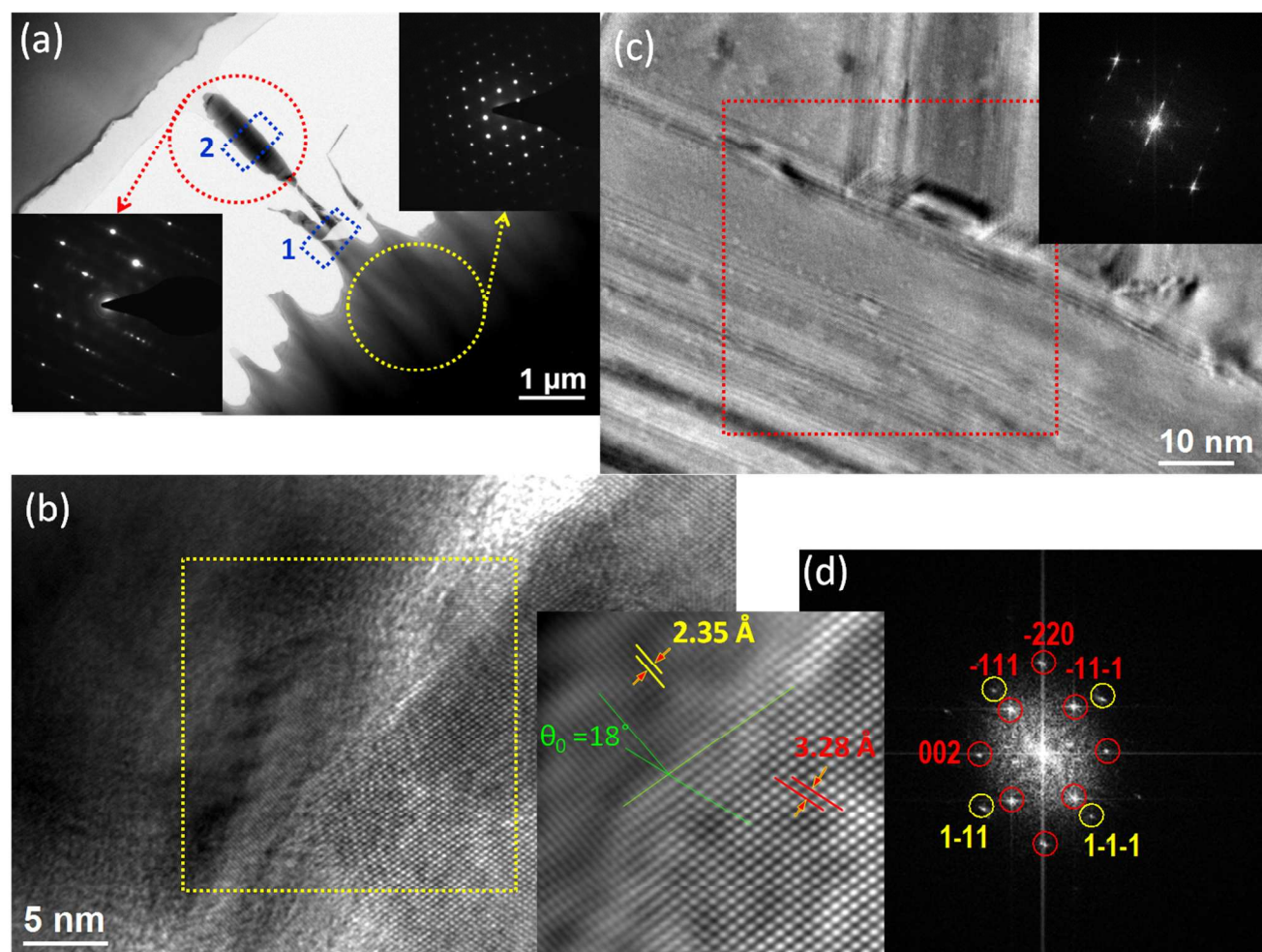


Fig. 3 (a) Low-magnification XTEM image of a typical Ag nanodendrite on Ge together with SAD patterns from the substrate and dendrite structure in the inset. (b) HRTEM image of the interface between Ag and Ge and Fourier filtered image in the inset clearly showing the overall tilt of the two lattices. (c) HRTEM image of the Ag nanodendrite together with FFT pattern in inset. (d) FFT pattern from the area marked in (b).

To understand further, we analyzed another set of Ag nanostructure on Ge substrate synthesized by identical chemical method but a much shorter growth time starting from 60 seconds to confirm if the tilted heteroepitaxy observed above is

maintained at the initial stage of growth. The XTEM image of a typical dendritic nanostructure for 2 minute growth is shown in Figure 4a at low magnification. Figure 4b is a HR-XTEM image from the interface between Ag nanodendrite and Ge substrate which shows a connection between the dendrite and the substrate and Figure 4c is a schematic showing how lattice tilt allows two lattices having mismatch coincide at the interface and similar interface between two mismatched cubic lattices. Number of misfit dislocation at the interface depends upon tilt angle, more the tilt angle, less the misfit dislocations. FFT pattern and Fourier filtered image in the inset of Figure 4b again indicates tilted epitaxy. We also observed that Ag(111) planes make a tilt of $\sim 28^\circ$ relative to the (111) planes of the Ge matrix which is 75% of the accommodation angle, meaning, samples grown for much short time can better accommodate the lattice mismatch than the samples grown for longer time through asymmetric tilt

boundaries in case of heteroepitaxy. Since maximum strain is accommodated by asymmetric tilt boundaries we have observed negligible misfit dislocation at the interface. However, the remaining strain is relaxed at top surface of Ag nanoparticles by introducing several defects (twining, stacking faults etc.) in the overgrown sample.

The phenomenon of titled hetero-epitaxial growth as observed in the present analysis is remarkable that violates our general wisdom on the basic mechanism of the solid state growth process. Our detail HRTEM based above mentioned analysis for the Ag-Ge interface indeed shows the direct evidence that growth of misfit-dislocation-free lattice-matched tilted epitaxial structures is possible where tilt boundaries can play an important role in accommodation of large lattice mismatch.

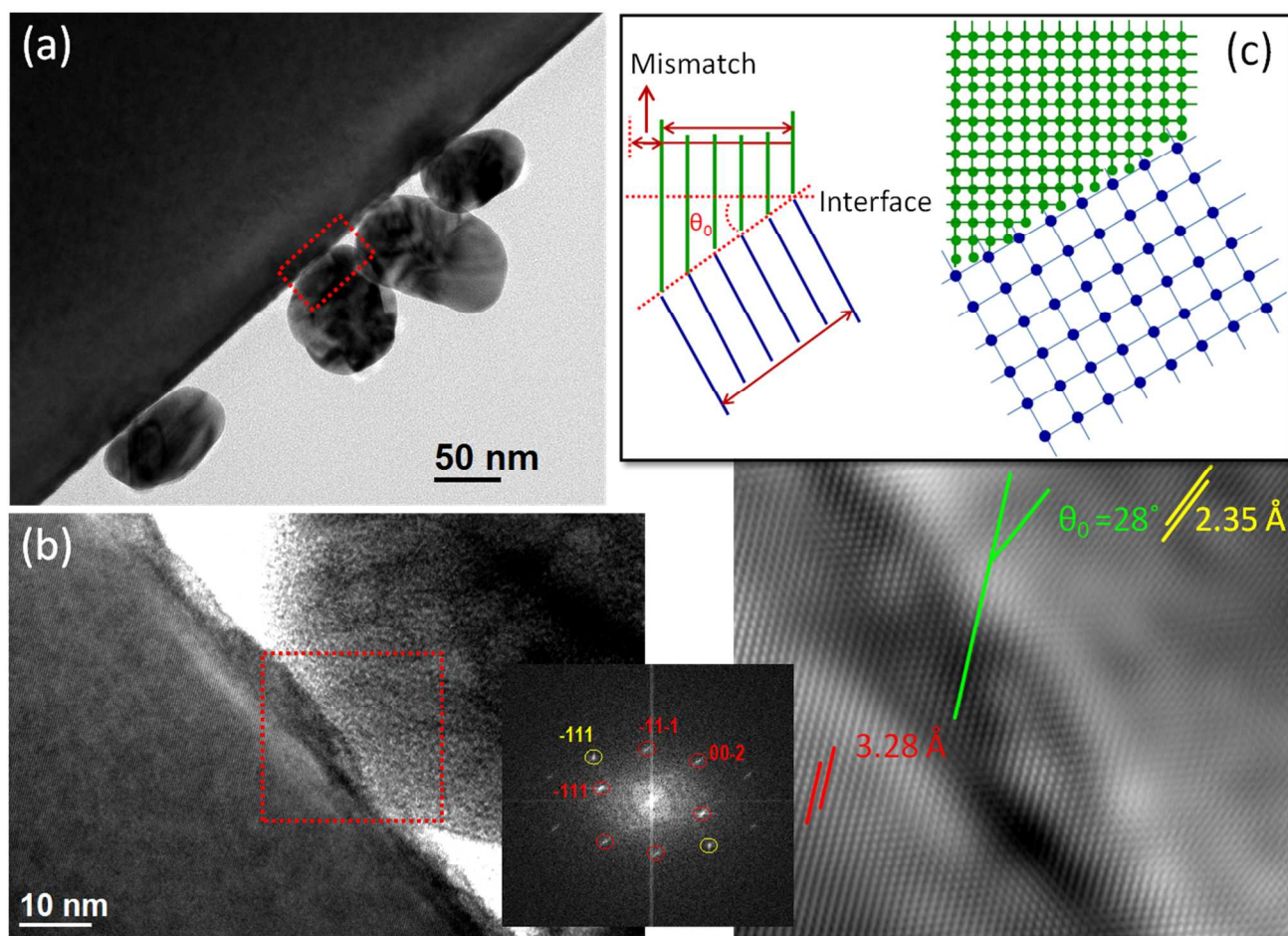


Fig. 4 (a) Typical low magnification XTEM image showing overall morphology after silver deposition on Ge (100) n-type wafer for 2 min, with 1 mM AgNO_3 . (b) HRTEM image of the interface marked by red dotted box in (a) and in the inset FFT patterns and Fourier filtered image. (c) Schematic (left) showing how lattice tilt allows two lattices having mismatch coincide at the interface and (right) similar interface between two mismatched cubic lattices.

Cite this: DOI: 10.1039/c0xx00000x

www.rsc.org/xxxxxx

ARTICLE TYPE

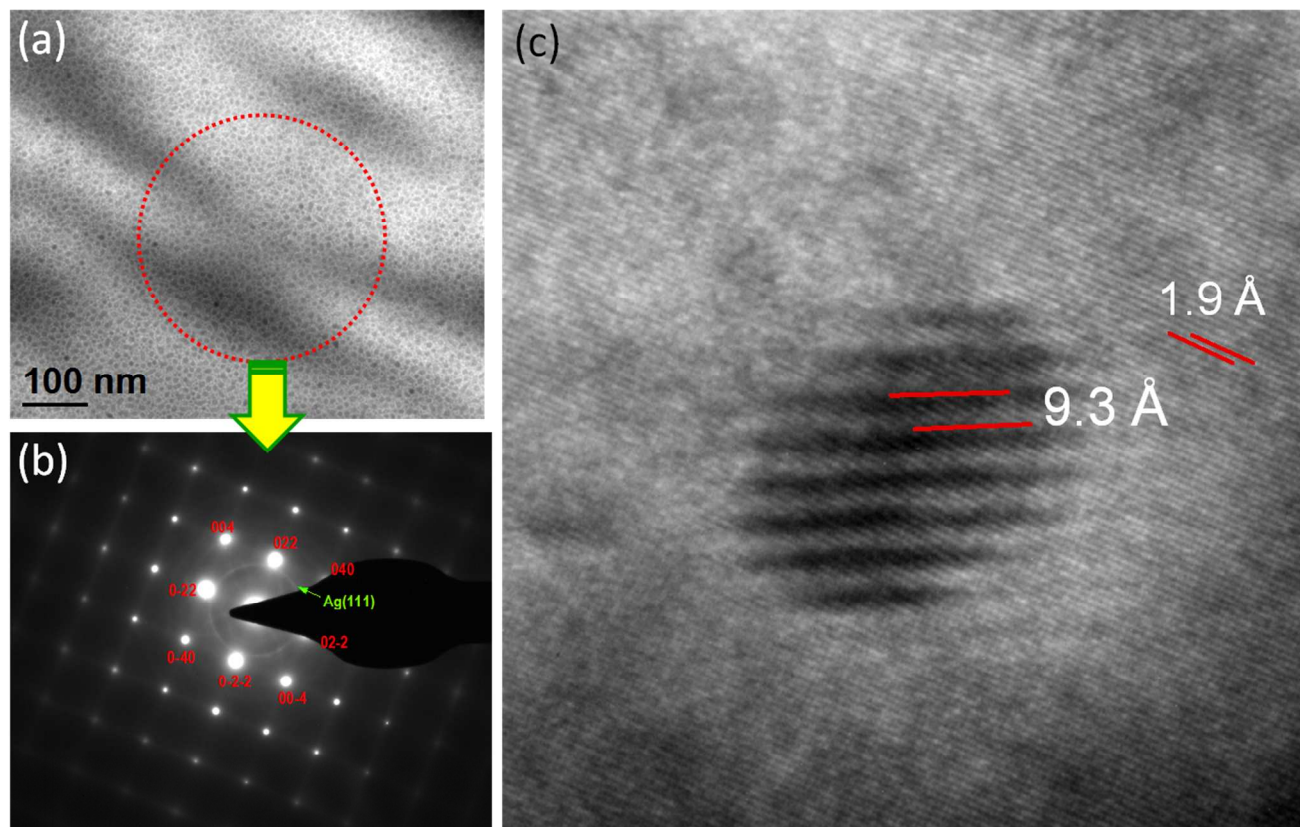


Fig. 5 (a) Plan-view TEM images of Ag films on Ge (100), produced after immersion for 1 min in 1 mM $\text{AgNO}_3(\text{aq})$. (b) Indexed single crystal (Ge) SAED pattern with ring pattern of Ag. Inter-planar spacing of ring is 2.36 Å. (c) HRTEM image shows Moiré pattern.

Further the plan-view TEM image of a typical dendritic nanostructure for 1 minute growth is shown in Figure 5a at low magnification. Figure 5b is a SAED pattern from same sample using large area aperture as shown by a dotted circle in 5a. HRTEM image from very small area of Figure 5a shows Moiré pattern resulting purely from the interference of two sets of planes. Here Moiré pattern is formed due to interference between Ge (220) with lattice spacing 1.99 Å and Ag (111) plane with lattice spacing 2.36 Å (as evident from SAED pattern of Figure 5b). The measured Moiré fringe spacing is 9.3 Å. If we consider general Moiré fringe with above mentioned lattice spacing the calculated value is 20.66 Å. Such difference can only be explained if the model of tilted epitaxial growth and lattice strain are considered.

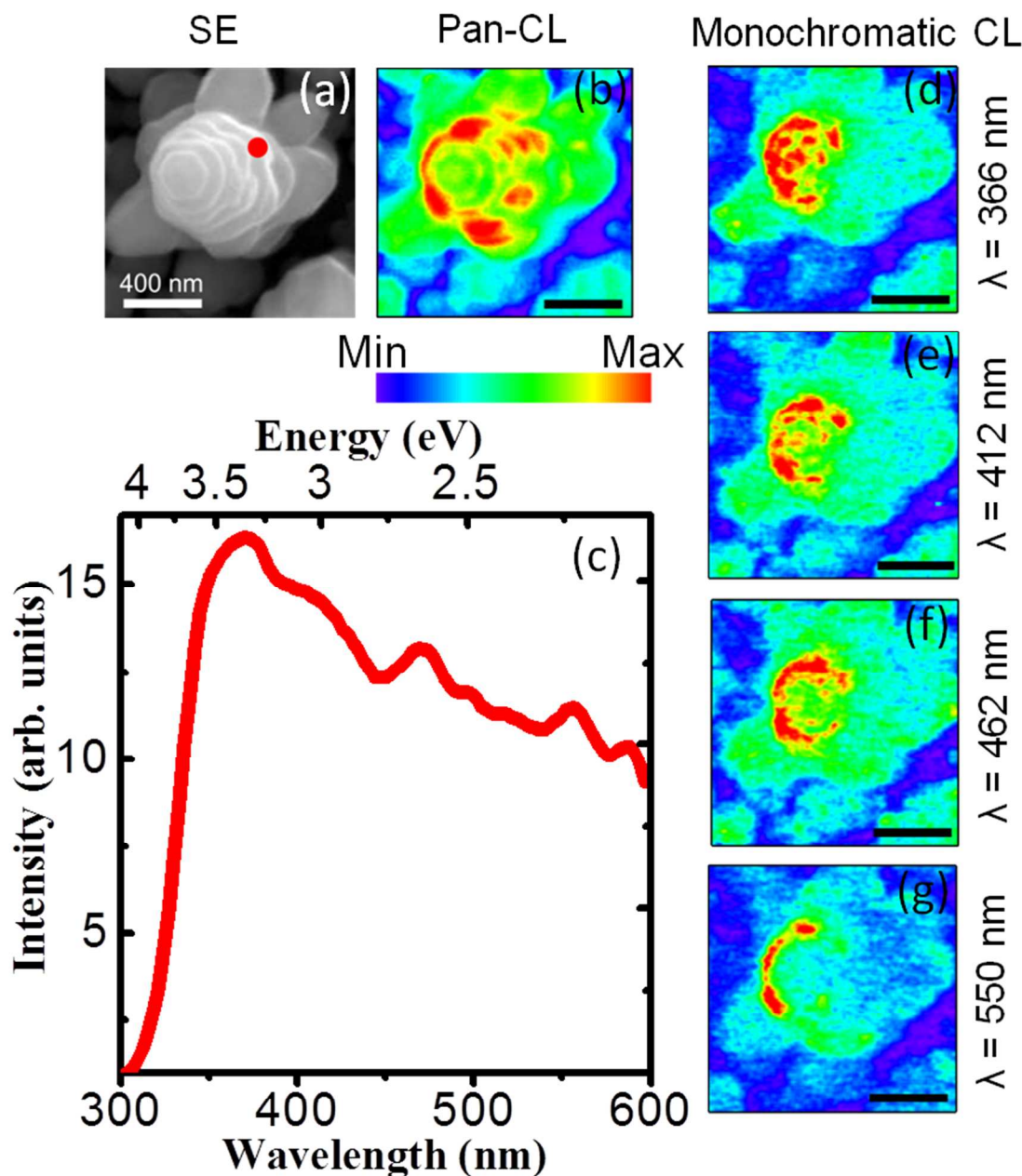
CL observation from a stack of hexagonal silver nanodisk

Yamamoto et al. first reported the use of electron irradiation to determine the spatially-resolved mode distribution of plasmons localized in silver nanoparticles.³⁴ However, experimental investigation on hexagonal nanodisks using electron irradiation

are not reported so far even though the theoretical study of the optical properties of silver nanodisks were published several years ago.³⁵ Among different kind of dendritic silver structures of the present sample, a typical nano-inukshuk in the form of stacked hexagons as shown in the SE image of Figure 6a was selected for CL study. In Figure 6b, we show the panchromatic CL map of this structure. It is interesting to note that the strongest photon emissions are observed when the electron beam is at the rounded corners of the stacked hexagons. The luminescence is also distinct along the side-edges of the hexagons. To obtain spectrally resolved features, we performed CL spectroscopy and imaging in the monochromatic mode. The CL spectrum shown in Figure 6c was acquired for the electron beam impact at a corner position (marked as red dot) of one of the hexagons of the stack. The CL spectrum of Figure 6c shows a strong peak at 366 nm (3.39 eV) which is close to the well-known surface plasmon peak of silver. A few other less intense peaks are also observed at wavelengths 412 nm, 462 nm and 550 nm. The monochromatic CL images (Figure 6d-g) recorded at four wavelengths, i.e., 366 nm, 412 nm, 462 nm and 550 nm show a clear trend that strong enhancement of light emission occurs when the electron beam

scans over the corners and edges of the Ag hexagons, the effect being most pronounced for the peak wavelength 366 nm. The luminescence intensity from the corners of the hexagons on the upper regions of the Ag nano-stacks is lost with increasing wavelengths. The spatial variations of the emission pattern as observed in the monochromatic photon maps in Figure 5 are a direct probe of resonant modes of plasmonic nanostructures and, consequently, provides a direct way to map the local electric fields. The spatial variation of emission here is caused when the field produced by the electron beam couples strongly when the electron beam is located near the largest electromagnetic fields of the resonant surface plasmon modes of a nanostructure. So we can identify the peak wavelengths 366 nm, 412 nm, 462 nm and 550 nm of the CL spectrum in Figure 6c as the resonant excitations. As the particles are sitting on a high index substrate,

the major dipolar mode of plasmon oscillation should be at IR regime, that is beyond the detection limit of our HSPMT detector.^{36, 37} The published literatures suggest that the most probable origin of the luminescence peaks at wavelengths 412 nm, 462 nm and 550 nm is due to the excitation of higher order (than the dipolar one) modes of plasmon oscillations. However, the dipolar and multipolar resonance peak positions are strongly related to the composition and specific features of the nano disk geometry.³⁴ It is emphasized that the present CL investigation reports to the best of our knowledge, the first experimental data on spectral and spatial profile of the photon emission from a stack of hexagonal silver nanodisks which may have strong impact on surface enhanced Raman scattering as will be discussed later in this paper.



30

Fig. 6 CL-SEM data. (a) Secondary electron (SE) image. (b) Panchromatic CL map of the same structure. (c) CL spectrum for the electron beam impact at a corner position (marked as red dot). (d-g) Monochromatic CL images recorded at four wavelengths, i.e., 366 nm, 412 nm, 462 nm and 550 nm.

SERS of Ag dendrites

Surface enhanced Raman scattering (SERS) is one of the most useful techniques for the future applications in diagnosis and single molecule sensing devices.³⁸⁻⁴⁰ Performance of SERS-based devices depends predominantly on SERS-active metal substrates that are usually colloidal silver nanoparticles randomly deposited on glass or silicon substrates. Large electromagnetic field enhancement generally occurs at SERS-active sites (“hot spots”) on colloidal nanoparticles such as in nanogaps, nanotips, sharp edges.⁴¹⁻⁴⁵ Because of their poor structural reproducibility and the easy oxidation and sulfuration, colloidal silver nanoparticles make serious obstacles to practical applications of SERS. Much effort has been devoted for developing high performance SERS substrates including silver nanostructures fabricated through lithographic technique^{46, 47} and the use of poly (vinyl alcohol) fibers⁴⁸ or three-dimensional (3D) nanoporous alumina membranes.⁴⁹ The problem with these techniques is that the fabrication procedure is very complicated and the SERS performance relies on the quality of both the membranes and the nanoparticles. As a better alternative to colloidal silver nanoparticles and complicated lithographic fabrication procedure, here we present a large-scale, simple dip-and-rinse fabrication approach to obtain a suitable SERS substrate with high performance. In the present case, using CL spectroscopy and imaging we have already shown (Figure 6) local field enhancements at the corners and edges of the hexagons justifying the use of present silver dendritic structure as a SERS active substrate. Figure 7a represents the SERS spectrum of 4-mercaptobenzoic acid in presence Ag dendrites which reveals the excellent electromagnetic field enhancement. High enhancement, i.e. SERS from Ag dendrites was also tested using Rhodamine 6G (Rh6G) as the analyte which is shown in Figure 7b. The enhancement factor (EF) of SERS signals may be calculated^{48,50} by a direct comparison using the equation, $EF = (I_{SERS}/I_{Raman}) \times$

$([N_{Bulk}]/[N_{Ads}])$, where I_{SERS} is the intensity of a certain vibrational mode in the SERS spectrum of analyte in the presence of nanoparticle, and I_{Raman} is the intensity of the same mode in the bulk Raman spectrum from the analyte alone. N_{Bulk} is the number of molecules used in the bulk, and N_{Ads} is the number of molecules adsorbed and sampled on the SERS-active substrate. All spectra are normalized for the integration time. The enhancement factor of SERS signal from 4-Mercaptobenzoic acid (for 1589 cm^{-1} vibrational mode) is estimated as 1×10^6 and that of using Rh6G (for 1651 cm^{-1} vibrational mode) is 4.5×10^7 . The enhancement factors of SERS signals from 4-Mercaptobenzoic acid and Rh6G are comparable to the literature values.^{48,51-54} Sufficient electromagnetic field enhancement is obtained due to several factors: (a) high surface-to-volume ratio of Ag dendrites which hold more number of analytes on their surface (b) enormous number of pointed corners and sharp edges of hexagonal units of Ag architectures offers the focusing of the electromagnetic field (surface plasmon) toward that specific locations (c) nanogaps between hexagonal units of a single Ag hexagonal-stack or between the hexagonal stacks residing on the Ge wafer with an excellent pattern at large areas, which trap dye molecules and form natural “hot spots”. Since surface structures can direct, channel, or focus the surface plasmons toward specific locations,⁵⁵ patterning over Ge surface can also provide a means to manipulate these plasmons and in turn SERS performance. So our silver dendrites, synthesized on Ge wafer, can be applied to fabricate highly effective SERS substrates in a very big way because of their ability of electromagnetic field enhancement. This type of Ag-based SERS substrate with superior reproducibility, excellent chemical stability, simple fabrication over large area with a patterned way, and easy manipulation promises to be an ideal candidate for a wide range of applications in sensing technology.

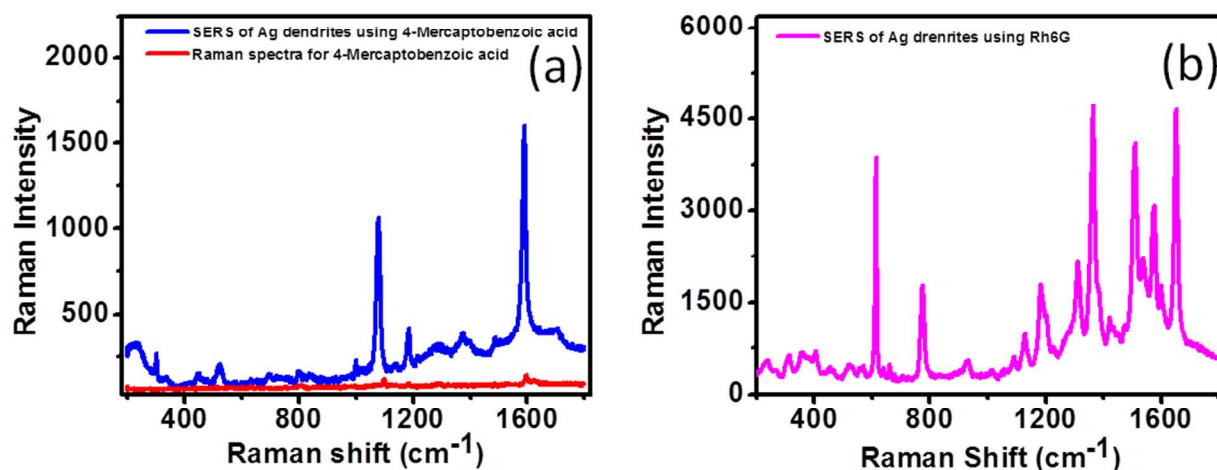


Fig. 7 SERS spectra of Ag dendrites on Ge for the two different analytes acquired using a laser excitation wavelength of 514 nm: (a) 4-Mercaptobenzoic acid, (b) Rhodamine 6G.

Cite this: DOI: 10.1039/c0xx00000x

www.rsc.org/xxxxxx

ARTICLE TYPE

Conclusions

We have studied the growth of dendritic silver nanostructures prepared by Galvanic displacement reaction directly on large-lattice-mismatched germanium surfaces and found a new type of heteroepitaxial growth where significantly large lattice mismatch is accommodated by formation of low-energy asymmetric tilt boundaries, which accommodate most of the strain without producing much misfit dislocations at the interface. This result suggests that growth of coincidence lattice-matched tilted structures should be possible in contrast to conventional heteroepitaxy where lattice mismatch is accommodated through biaxial strain and interfacial misfit dislocations. Larger tilt angle introduce less misfit dislocation at the interface. This mode of accommodation of lattice mismatch should substantially expand the class of material combinations available for practical applications such as SERS active substrate. Our work provides a very simple, convenient, cost-effective, and fast route to synthesize Ag dendrites which is potentially useful in nano plasmonics and sensing application.

ACKNOWLEDGEMENT

Authors thankfully acknowledge the help of Manash Ghosh, IACS, Kolkata in SERS measurements and Dr. Dulal Senapati, CSD, SINP for useful discussions.

Notes and references

Saha Institute of Nuclear Physics, 1/AF Bidhannagar, Kolkata-700 064, India. E-mail: biswarup.satapati@saha.ac.in

- 1 D. J. Milliron, S. M. Hughes, Y. Cui, L. Manna, J. B. Li, L. W. Wang and A. P. Alivisatos, *Nature*, 2004, **430**, 190.
- 2 H. X. Xu, E. J. Bjerneld, M. Kall and M. Borjesson, *Phys. Rev. Lett.*, 1999, **83**, 4357.
- 3 T. Huang, F. Meng and L. Qi, *Langmuir*, 2010, **26**, 7582.
- 4 J. Ye, L. Lagae, G. Maes, G. Borghs and P. Van Dorpe, *Optics Express*, 2009, **17**, 23765.
- 5 E. Prodan, C. Radloff, N. J. Halas and P. Nordlander, *Science*, 2003, **302**, 419.
- 6 Y. K. Wang, T. Y. Yang, M. T. Tuominen and M. Achermann, *Phys. Rev. Lett.*, 2009, **102**, 163001.
- 7 H. A. Atwater and A. Polman, *Nat. Mater.*, 2010, **9**, 205.
- 8 M. Micic, N. Klymyshyn and H. P. Lu, *J. Phys. Chem. B*, 2004, **108**, 2939.
- 9 C. Gu and T. Y. Zhang, *Langmuir*, 2008, **24**, 12010.
- 10 Q. Zhou, S. Wang, N. Jia, L. Liu, J. Yang and Z. Jiang, *Mater. Lett.*, 2006, **60**, 3789.
- 11 V. M. Maksimović, M. G. Pavlović, L. J. Pavlović, M. V. Tomić and V. D. Jović, *Hydrometallurgy*, 2007, **86**, 22.
- 12 L. Qian and X. Yang, *Colloids Surf. A*, 2008, **317**, 528.
- 13 W. Song, Y. Cheng, H. Jia, W. Xu and B. J. Zhao, *Colloid Interface Sci.*, 2006, **298**, 765.
- 14 X. Wen, Y. T. Xie, M. W. C. Mak, K. Y. Cheung, X.-Y. Li, R. Renneberg and S. Yang, *Langmuir*, 2006, **22**, 4836.
- 15 J. Fang, H. You, P. Kong, Y. Yi, X. Song and B. Ding, *Cryst. Growth Des.*, 2007, **7**, 864.

- 16 A. Gütés, C. Carraro and R. Maboudian, *J. Am. Chem. Soc.*, 2010, **132**, 1476.
- 17 J. Fang, B. Ding and X. Song, *Cryst. Growth Des.*, 2008, **8**, 3616.
- 18 G. Wei, C. W. Nan, Y. Deng and Y. H. Lin, *Chem. Mater.*, 2003, **15**, 4436.
- 19 Y. Zhu, H. Zheng, Y. Li, L. Gao, Z. Yang and Y. Qian, *Mater. Res. Bull.*, 2003, **38**, 1829.
- 20 Z. Wang, Z. Zhao and J. Qiu, *J. Phys. Chem. Solids*, 2008, **69**, 1296.
- 21 G. J. Lee, S. I. Shin and S. G. Oh, *Chem. Lett.*, 2004, **33**, 118.
- 22 G.-H. Jiang, L. Wang, T. Chen, H.-J. Yu and J. J. Wang, *J. Mater. Sci.*, 2005, **40**, 1681.
- 23 P. S. Mdluli and N. Revaprasadu, *Mater. Lett.*, 2009, **63**, 447.
- 24 J. P. Xiao, Y. Xie, R. Tang, M. Chen and X. Tian, *Adv. Mater.*, 2001, **13**, 1887.
- 25 Y. Zhou, S. H. Yu, C. Y. Wang, X. G. Li, Y. R. Zhu and Z. Y. Chen, *Adv. Mater.*, 1999, **11**, 850.
- 26 Z. Wang, F. Tao, D. Chen, L. Yao, W. Cai and X. Li, *Chem. Lett.*, 2007, **36**, 672.
- 27 X. Chen, Chun-Hua Cui, Z. Guo, Jin-Huai Liu, Xing-Jiu Huang and Shu-Hong Yu, *small* 2011, **7**, 858.
- 28 D. Grozea, E. Bengu and L. D. Marks, *Surf. Sci.*, 2000, **461**, 23.
- 29 M. Aizawa, A. M. Cooper, M. Malac and J. M. Buriak, *Nano Lett.*, 2005, **5**, 815.
- 30 P. Das and T. K. Chini, *Current Science*, 2011, **101**, 849.
- 31 M. Kuttge, E. J. R. Vesseur, A. F. Koenderink, H. J. Lezec, H. A. Atwater, F. J. García de Abajo and A. Polman, *Phys. Rev. B*, 2009, **79**, 113405.
- 32 E. J. R. Vesseur, R. de Waele, M. Kuttge and A. Polman, *Nano Lett.*, 2007, **7**, 2843.
- 33 B. W. Dodson, D. R. Myers, A. K. Datye, V. S. Kaushik, D. L. Kendall and B. Martinez-Tovar, *Phys. Rev. Lett.*, 1988, **61**, 2681.
- 34 N. Yamamoto, K. Araya and F. J. García de Abajo, *Phys. Rev. B*, 2001, **64**, 205419.
- 35 A. Brioude and M. P. Pileni, *J. Phys. Chem. B*, 2005, **109**, 23371.
- 36 P. Das, T. K. Chini and J. Pond, *J. Phys. Chem. C*, 2012, **116**, 15610.
- 37 P. K. Chaturvedi, K. H. Hsu, A. Kumar, K. H. Fung, J. C. Mabon and N. X. Fang, *ACS Nano*, 2009, **3**, 2965.
- 38 R. A. Alvarez-Puebla and L. M. Liz-Marzán, *Small*, 2010, **6**, 604.
- 39 P. J. Vikesland and K. R. Wigginton, *Environ. Sci. Technol.*, 2010, **44**, 3656.
- 40 H. Liu, L. Zhang, X. Lang, Y. Yamaguchi, H. Iwasaki, Y. Inouye and Q. Xue, *Scientific Reports*, 2011, **1**:1121.
- 41 Dong-Kwon Lim, Ki-Seok Jeon, H. M. Kim, Jwa-Min Nam and Y. D. Suh, *Nat. Mater.*, 2010, **9**, 60.
- 42 S. L. Kleinman, E. Ringe, N. Valley, K. L. Wustholz, E. Phillips, K. A. Scheidt, G. C. Schatz and R. P. V. Duyne, *J. Am. Chem. Soc.*, 2011, **133**, 4115.
- 43 L. Rodriguez-Lorenzo, R. A. Álvarez-Puebla, I. Pastoriza-Santos, S. Mazzucco, O. Stéphan, M. Kociak, L. M. Liz-Marzán and F. J. García de Abajo, *J. Am. Chem. Soc.*, 2009, **131**, 4616.
- 44 Dong-Kwon Lim, Ki-Seok Jeon, Jae-Ho Hwang, H. Kim, S. Kwon, Y. D. Suh and Jwa-Min Nam, *Nat. Nanotech.*, 2011, **6**, 452.
- 45 J. F. Li, Y. F. Huang, Y. Ding, Z. L. Yang, S. B. Li, X. S. Zhou, F. R. Fan, W. Zhang, Z. Y. Zhou, D. Y. Wu, Z. L. Wang and Z. Q. Tian, *Nature*, 2010, **464**, 392.
- 46 Y. Sawai, B. Takimoto, H. Nabika and K. Murakoshi, *J. Am. Chem. Soc.*, 2007, **129**, 1658.
- 47 N. A. Hatab, C. H. Hsueh, A. L. Gaddis, S. T. Retterer, J. H. Li, G. Eres, Z. Zhang and B. Gu, *Nano Lett.*, 2010, **10**, 4952.
- 48 D. He, B. Hu, Q. F. Yao, K. Wang and S. H. Yu, *ACS Nano*, 2009, **3**, 3393.
- 49 H. Ko, S. Chang and V. V. Tsukruk, *ACS Nano*, 2009, **3**, 181.
- 50 H. J. Yang, S. Y. He and H. Y. Tuan, *Langmuir*, 2014, **30**, 602.

-
- 51 W. Song, Y. Cheng, H. Jia, W. Xu and B. Zhao, *J. Colloid Interface Sci.*, 2006, **298**, 765.
- 52 L. He, M. Lin, H. Lib and N. J. Kim, *J. Raman Spectrosc.*, 2010, **41**, 739.
- 53 B. Zhang, H. Wang, L. Lu, K. Ai, G. Zhang and X. Cheng, *Adv. Funct. Mater.*, 2008, **18**, 2348.
- 54 S. H. Ciou, Y. W. Cao, H. C. Huang, D. Y. Su and C. L. Huang, *J. Phys. Chem. C*, 2009, **113**, 9520.
- 55 P. Nagpal, N. C. Lindquist, S. H. Oh and D. J. Norris, *Science*, 2009, **325**, 594.